



Photocatalytic degradation of rhodamine B using Mo heterogeneous catalysts under aerobic conditions

Nuno U. Silva^a, Teresa G. Nunes^b, Marta S. Saraiva^a, Mohammad S. Shalamzari^a, Pedro D. Vaz^{a,**}, Olinda C. Monteiro^a, Carla D. Nunes^{a,*}

^a CQB, Departamento de Química e Bioquímica, Faculdade de Ciências, Universidade de Lisboa, 1749-016 Lisboa, Portugal

^b CQE, Instituto Superior Técnico, Universidade Técnica de Lisboa, Av. Rovisco Pais, 1049-001 Lisboa, Portugal

ARTICLE INFO

Article history:

Received 22 September 2011

Received in revised form

16 November 2011

Accepted 18 November 2011

Available online 30 November 2011

Keywords:

DFT

Dye

MCM-41

Molybdenum

Catalysis

ABSTRACT

MCM-41 based materials were prepared with immobilized Mo^{II} and Mo^{VI} active sites based on [Mo₂(CO)₃] and [MoO₂Cl₂] cores, respectively, using a 2-aminopyridine glycidylxypropyl derivative as anchoring ligand. Suitable characterization by powder X-ray diffraction, FTIR and, ¹³C and ²⁹Si solid state NMR spectroscopy was accomplished. All new materials were successfully used in photodegradation experiments of rhodamine B under aerobic conditions. Control experiments using neat MCM-41 and direct photolysis of rhodamine B were also carried out. All experiments were run without any external source of oxygen other than air. Photocatalytic results show that the presence of Mo and its oxidation state is not innocent in this process. In addition, Mo catalysts act most probably by quenching rhodamine B excited state leading to extended degradation of the dye, through secondary photochemistry, beyond a simple de-ethylation process. Density functional theory (DFT) results corroborate with this showing that when rhodamine B is in excited state the xanthene moiety bond orders change.

© 2011 Elsevier B.V. All rights reserved.

1. Introduction

Since the discovery of the periodic mesoporous molecular sieves of the M41S family by researchers at Mobil in 1992 [1], a new era in inclusion chemistry began [2]. It is now obvious that morphological control and texture of mesoporous silica, though extremely important for diverse applications [3,4], is now easily achieved [5]. Mesoporous materials are synthesized using surfactants (and co-surfactants) as structure directing agents, around which a source of the building blocks of interest, e.g. sodium silicate, will polymerize yielding the mesoporous structure after proper ageing under hydrothermal conditions. This results in materials that are attractive due to the considerably large pores when compared with zeolites making them ideal for guest molecules uptake [1,6].

MCM-41, one of the members of the M41S family, possesses a high surface area, an ordered framework and a narrow pore size distribution. These structural features give MCM-41 potential applications as host material, catalyst for reactions involving large

molecules and as chromatographic material [7,8]. The mesoporous materials are of great interest for catalytic applications due to their large and uniform pores that can be used as hosts for incorporation of different metals, creating and enlarging the activity inside the porous frameworks. Until now, three processes have been reported for active site introduction in mesoporous materials: (1) one-pot synthesis [9–11], in which metal organic or inorganic precursors are directly added in the parent silicon sol whereby the metal becomes part of the wall structure; (2) template-ion exchange [12], in which the template ions of the as-prepared materials are exchanged with other metal ions in solution; and (3) post-synthesis modification in which the abundant surface Si–OH bonds of calcined materials react with (organo)metallic complexes or other metal compounds [13–16]. Specific surface properties can be tailored by either proper surface modifications [9] or isomorphous substitution of Si atoms by tri- (Al, B) or tetravalent (Ge) metal cations [10–12].

In recent years attention has been drawn to pollutant remediation processes. The development of techniques to accomplish such end is still an area under strong development, given the plethora of pollutant systems to deal with. In the particular case of textile industry, dye pollutants are a dangerous source of environmental contaminants owing to their resistance to biodegradation [16,17]. Several useful processes such as sonolysis [18], photocatalysis [19–21] and (photo-)Fenton reactions [22–24] have emerged as adequate approaches for the decomposition of organic compounds in acidic or neutral media. However, reports concerning the

* Corresponding author at: CQB, Departamento de Química e Bioquímica, Faculdade de Ciências, Universidade de Lisboa, 1749-016 Lisboa, Portugal. Tel.: +351 217 500 876; fax: +351 217 500 088.

** Corresponding author at: CQB, Departamento de Química e Bioquímica, Faculdade de Ciências, Universidade de Lisboa, 1749-016 Lisboa, Portugal. Tel.: +351 217 500 877; fax: +351 217 500 088.

E-mail addresses: pmvaz@fc.ul.pt (P.D. Vaz), cmnunes@fc.ul.pt (C.D. Nunes).

degradation of dyes under alkaline conditions, especially at higher pH values, are rare [25–29].

Usually, the catalysts used in these processes are inorganic materials either as bulk, nanoparticles, films or colloids. Some of the above mentioned degradation processes require the use of an oxidant component, usually H_2O_2 , besides the catalyst [30–34]. Nevertheless this fact is associated with an increase on the process control complexity.

Nanocrystalline TiO_2 is nowadays the semiconductor material most used as photocatalyst for the treatment of industrial wastewaters. However, the major drawbacks for its wide practical application are its high charge recombination rate and its wide band gap (anatase, ca. 3.2 eV) which limits the photogeneration of electrons and holes to the UV light below 387 nm (only ~5% of the solar radiation reaching the Earth).

As a result, the development of new visible light responsive photocatalysts and the improvement of charge separation and minimization of charge-carrier recombination are important goals to achieve in this active research area. An enhancement on TiO_2 photocatalytic properties can be obtained by doping it with Mo^{VI} species. In this case an increase in the rate of transfer of electrons from the TiO_2 via the formation of a reduced molybdenum species was observed [35]. In this way, due to its redox properties, the Mo based materials can be found as an alternative to TiO_2 in order to develop higher efficient photocatalytic materials. The use of such catalysts takes advantage of the tunable band-gap which offers tailored solutions for a given purpose being TiO_2 one of the most used.

In this work a study on the photodegradation of rhodamine B (rhB), a model dye, using MCM-41 materials derivatized with Mo^{II} and Mo^{VI} active sites, is presented. Mo is known to act as active catalyst in photocatalytic oxygen transfer reactions [36–40]. The Mo-containing MCM materials take advantage of both the support high surface area, ca. $1000\text{ m}^2\text{ g}^{-1}$, and the Mo centers photocatalytic properties. To this respect the high surface area is advantageous not only enabling MCM-41 to act as a mass transfer agent, but also by ensuring the maximum contact between the dye and the active sites.

2. Experimental

2.1. General

All reagents were obtained from Aldrich and used as received. Commercial grade solvents were dried and deoxygenated by standard procedures (thf and toluene over Na/benzophenoneketyl; CH_3OH over magnesium; CH_3CN over CaH_2), distilled under nitrogen, and kept over 4 Å molecular sieves. The complexes $[\text{Mo}_2(\text{CO})_3(\text{NCMe})_2]$ and $[\text{MoO}_2\text{Cl}_2(\text{thf})_2]$ were prepared according to literature methods [41,42]. Two batches of MCM-41 (**2**, **2***) were synthesized, one for each Mo species (* denotes the second batch). Both MCM-41 (**2**, **2***) were synthesized by adopting a methodology previously described, using $[(\text{C}_{14}\text{H}_{33})\text{N}(\text{CH}_3)_3]\text{Br}$ as structure directing agent [43]. Template molecules were removed by calcination at 813 K for 6 h under air. Prior to grafting experiments, physisorbed water was removed from calcined MCM by heating at 180 °C in vacuum (10^{-2} Pa) for 2 h.

FTIR spectra were acquired with a Nicolet 6700 fitted with a Smart-diffuse reflectance (DRIFT) accessory. Spectra were measured in the 400–4000 cm^{-1} range using 2 cm^{-1} resolution.

UV–vis spectra were measured with a Shimadzu UV-2450PC spectrometer. All spectra were measured using H_2O as solvent in the 190–900 nm range.

Powder XRD measurements were taken on a Philips PW1710 using $\text{Cu-K}\alpha$ radiation filtered by graphite.

^1H and ^{13}C solution NMR spectra were obtained with a Bruker-Avance 400 spectrometer.

Solid state NMR (SS-NMR) measurements were performed at room temperature on a Bruker MSL 300P spectrometer operating at 59.60 and 75.47 MHz for the observation of ^{29}Si and ^{13}C resonances, respectively. The standard magic angle spinning (MAS) cross polarization–dipolar decoupling RF pulse sequence (CP-DD) was used under about 4 kHz spinning rate. For the acquisition of ^{29}Si spectra, 5 ms contact time, 6 s recycling delay and a number of scans always higher than 3000 were selected; the Hartmann–Hahn condition was optimized using tetrakis-trimethylsilyl-silane and tetramethylsilane (tms) was the external reference to set the chemical shift scale ($\delta=0$). ^{13}C spectra were recorded with 2 ms contact time, 4 s recycling delay and a number of scans higher than 900. The Hartmann–Hahn condition was optimized using glycine, also the external reference to set the chemical shift scale (^{13}CO at 176.1 ppm).

The N_2 sorption measurements were obtained in an automatic apparatus (ASAP 2010; Micromeritics). BET specific surface areas (S_{BET} , p/p_0 from 0.03 to 0.13) and specific total pore volume, V_p , were estimated from N_2 adsorption isotherms measured at 77 K. The pore size distributions (PSD) were calculated by the BJH method using the modified Kelvin equation with correction for the statistical film thickness on the pore walls [44,45]. The statistical film thickness was calculated using Harkins–Jura equation in the p/p_0 range from 0.1 to 0.95.

Microanalyses for CHN and Mo quantification were performed at CACTI, University of Vigo. CHN analyses were performed on a Fisons EA 1108; Mo quantification was performed on a Perkin Elmer Optima 4300DV using In as internal standard.

The detection and identification of compounds resulting from the catalytic photodegradation experiments was accomplished by electrospray mass spectrometry (ESI-MS). Such experiments were performed on a LCQ Duo ion trap mass spectrometer from Thermo Finnigan (San Jose, CA, USA). Samples were introduced, via a syringe pump (flow rate of 5 mL/min), into the stainless steel capillary of the ESI source. All mass spectrometry data were acquired in positive ion mode, the full scan spectra were recorded in the range m/z 50–600 and the applied spray voltage in the source was 4.5 kV, the capillary voltage was 10 V and the capillary temperature was 493 K using N_2 both as nebulizing and drying gas in the source. MS^2 experiments were performed with He from Praxair (Danbury, CT, USA), at various resonant excitation amplitude values requiring excitation voltages in the range 0.75–1.75 V_{pp} . The collision energy was gradually increased until the precursor and the product ions could, both, be observed in the MS^2 spectrum.

2.2. Methods

2.2.1. Glypy (**1**)

A solution of (3-glycidyloxypropyl)trimethoxysilane (2.25 ml, 10 mmol) in MeOH (10 ml) was added to a solution of 2-aminopyridine (0.98 g, 10 mmol) in 15 ml MeOH. After 12 h at 348 K the solution was evaporated in vacuum to give a yellow–brown oil product (2.94 g) in 93% yield.

Elemental analysis (%) $\text{C}_{14}\text{H}_{25}\text{N}_2\text{O}_5\text{Si}$ (339.15): calcd. C 51.04, H 7.65, N 8.50; found: C 50.64, H 8.00, N 8.65.

IR (KBr ν/cm^{-1}): 3354 (s), 3197 (s), 2940 (vs), 2840 (vs), 1646 (vs), 1622 (vs), 1195 (vs), 1089 (vs).

^1H NMR (400.13 MHz, CDCl_3 , r.t., δ ppm, J Hz): 8.06 (d, H_6 , $^3J_{\text{HH}}=4.00$), 7.41 (t, H_4 , $^3J_{\text{HH}}=8.00$), 6.63 (t, H_5 , $^3J_{\text{HH}}=4.00$), 6.49 (d, H_3 , $^3J_{\text{HH}}=8.00$), 4.20 (s bd, H_8), 3.90 (s, NH), 3.56 (s, OCH_3), 3.34–3.49 (m, H_{7a} , H_{7b} , H_{9a} , H_{9b} , H_{10} , OH), 1.68 (m, H_{11}), 0.66 (s, H_{12}).

^{13}C NMR (100.62 MHz, CDCl_3 , r.t., δ ppm): 158.4 (C_2), 148.1 (C_6), 137.7 (C_4), 114.0 (C_5), 108.5 (C_3), 103.1 (C_8), 73.8 (C_{10}), 59.3 (C_9), 57.3 (C_7), 50.5 (OCH_3), 24.0 (C_{11}), 7.1 (C_{12}).

2.2.2. MCM-glypy (3, 3*)

A solution of glypy (**1**) (0.387 g, 1.1 mmol) in toluene (10 mL) was added to a MCM-41 suspension (1 g) in toluene (10 mL), and the mixture was heated at 373 K for 9 h. The resulting solid was filtered off and washed four times with CH₂Cl₂ (4 × 15 mL), then dried in vacuum at 323 K for 2 h.

2.2.2.1. (3) Elemental analysis (%): found C 10.96, H 2.03, N 1.38. IR (ν/cm^{-1}): 3904 (w), 3854 (w), 3840 (w), 3752 (w), 3676 (w), 3400 (s), 3240 (f), 2930 (m), 1654 (m), 1628 (m), 1240 (vs), 1079 (vs), 800 (s).

²⁹Si CP MAS NMR (δ ppm): –50 (*T*¹), –57 (*T*²), –67 (*T*³), –100 (*Q*³), –110 (*Q*⁴).

¹³C CP MAS NMR (δ ppm): 143.1, 128.3, 124.8 (pyridine moiety), 73.9 (*C*₁₀), 57.3 (*C*₉, *C*₇), 22.2 (*C*₁₁), 8.2 (*C*₁₂).

2.2.2.2. (3*) Elemental analysis (%): found C 11.91, H 1.98, N 1.22. IR (ν/cm^{-1}): 3440 (s), 3260 (f), 2950 (m), 1630 (m), 1628 (s), 1590 (w), 1490 (w), 1450 (m), 1250 (vs), 1100 (vs), 818 (s).

²⁹Si CP MAS NMR (δ ppm): –57 (*T*²), –67 (*T*³), –92 (*Q*²), –102 (*Q*³), –109 (*Q*⁴).

¹³C CP MAS NMR (δ ppm): 143.1, 128.3, 125.0 (pyridine moiety), 73.6 (*C*₁₀), 58.2 (*C*₉, *C*₇), 48.4 (OCH₃), 22.2 (*C*₁₁), 8.4 (*C*₁₂).

2.2.3. MCM-glypy-Mo^{II} (4)

A solution of [MoI₂(CO)₃(NCMe)₂] (0.335 g, 0.65 mmol) in dry CH₂Cl₂ (5 mL) was added to a suspension of 0.9 g of MCM-glypy (**3**) material in dry CH₂Cl₂ (15 mL). The reaction mixture was stirred under a N₂ atmosphere at room temperature overnight. The resulting material was then filtered off, washed twice with CH₂Cl₂ (3 × 20 mL), and dried under vacuum for 3 h.

Elemental analysis (%): found C 9.44, H 1.65, N 0.88, Mo 1.80. IR (ν/cm^{-1}): 3748 (w), 3383 (vs), 2941 (m), 2030 (w), 1960 (w), 1880 (w), 1668 (s), 1634 (s), 1240 (vs), 1070 (vs), 969 (m).

²⁹Si CP MAS NMR (δ ppm): –56 (*T*²), –65 (*T*³), –100.7 (*Q*³), –109.3 (*Q*⁴).

¹³C CP MAS NMR (δ ppm): 154.5, 142.9 (pyridine moiety), 73.7 (*C*₁₀), 59.2 (*C*₉, *C*₇), 22.4 (*C*₁₁), 8.8 (*C*₁₂).

2.2.4. MCM-glypy-Mo^{VI} (5)

A solution of [MoO₂Cl₂(thf)₂] (0.52 g, 1.5 mmol) in CH₂Cl₂ (5 mL) was added to a suspension of the MCM-glypy (**3**) (1.0 g) in CH₂Cl₂ (10 mL) and the mixture stirred overnight at room temperature. The resultant solid was then filtered off and washed with CH₂Cl₂ (3 × 20 mL), and dried in vacuum at room temperature for 3 h.

Elemental analysis (%): found C 8.98, H 1.76, N 0.99, Mo 4.62. IR (ν/cm^{-1}): 3744 (w), 3407 (vs), 2950 (w), 2900 (w), 1667 (s), 1629 (s), 1240 (vs), 1081 (vs), 958 (m), 939 (m).

²⁹Si CP MAS NMR (δ ppm): –58 (*T*²), –69 (*T*³), –101 (*Q*³), –109 (*Q*⁴).

¹³C CP MAS NMR (δ ppm): 154.5, 143.1 (pyridine moiety), 73.6 (*C*₁₀), 67.5 (*C*₉), 58.6 (*C*₇), 22.4 (*C*₁₁), 9.3 (*C*₁₂).

2.3. DFT calculations

Density functional theory (DFT) calculations [46] were performed using the Gaussian 03 program (rev. C02) [47], with the B3LYP hybrid functional, which includes a mixture of Hartree–Fock exchange with DFT exchange–correlation given by Becke's three parameter hybrid functional with Lee Yang and Parr's gradient-corrected correlation functional [48]. The 6-311G** basis set [49] was used on all atoms. The starting geometry of rhB was based on spectroscopic data and optimized without any symmetry constraints. Frequency calculations were performed at the same level of theory to confirm the nature of the stationary points, yielding no imaginary frequencies for the minima. The 40 lowest energy

excitations were obtained from time-dependent (TD) calculations, carried out at the same level of theory, using the TD keyword of Gaussian 03 [50]. NBO analyses were performed with the GENNBO 5.0 algorithm [51].

2.4. Photocatalytic degradation experiments

The photodegradation experiments have been conducted using an Ace Glass photoreactor cooled by water circulation. The reaction vessel (250 mL) is made of borosilicate glass and suitable to accommodate an immersion well. The quartz immersion well, is double-walled, with inlet and outlet tubes for cooling. The inlet tube extends down the annular space and ensures the upward flow of coolant from the bottom of the well upward to the outlet. The reactor has one angled joint for the sparger tube, one vertical joint for the condenser and one Ace-Thread side arm for the thermometer. The reactor bottom is flat to allow the use of a magnetic stirrer. The radiation source was a 450 W medium pressure mercury vapor lamp (from Hanovia). Of the total radiated energy, approximately 40–48% is in the ultraviolet portion of the spectrum and 40–43% in the visible. The radiated watt density is 0.37 W/cm².

Suspensions have been prepared by adding 150 mg of a given nanocomposite powder to 150 mL of 20 ppm rhB aqueous solution, at neutral pH. Prior to irradiation, the suspensions were stirred under dark conditions for 2 h to reach sorption/desorption equilibrium. The rhB photodegradation in the absence of catalyst (photolysis) has been also evaluated.

During irradiation, the suspensions were sampled at regular intervals. The concentrations of the rhB solutions were calculated by measuring their absorbance at the maximum absorption peak (554 nm). The identification of the degradation products was done by ESI-MS.

3. Results and discussion

3.1. Synthesis of anchoring ligand

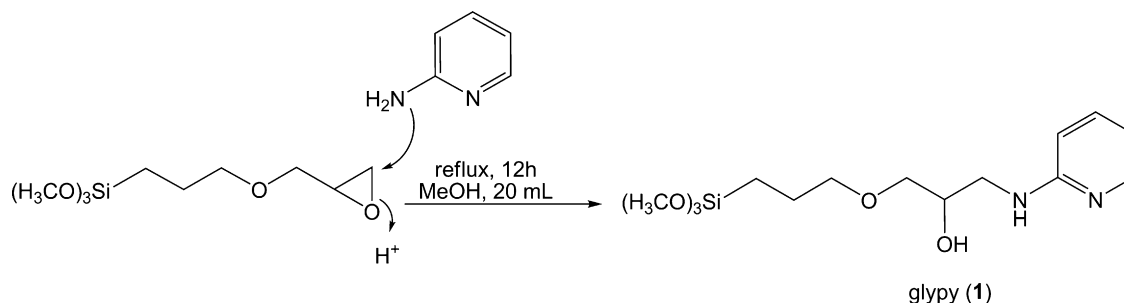
Ligand **1**, prepared during this work was obtained in 93% yield, from the reaction between 2-aminopyridine and (3-glycidyloxypropyl)trimethoxysilane, in MeOH being formulated as C₁₄H₂₅N₂O₅Si [52], according to Scheme 1.

Formation of **1** was certified by FTIR namely the new broad band assigned to the $\nu\text{Si-O}$ and $\nu\text{C-O-C}$ modes of the ligand at 1089 and 1195 cm^{–1}. Also new bands from νNH and νOH modes at 3197 cm^{–1} and at 3354 cm^{–1} are observed indicating the reaction success. The concomitant disappearing of the band due to the oxirane ring at 1256 cm^{–1} is also indicative that the reaction was accomplished.

The spectroscopic characterization of **1** was also performed by solution NMR (Table S1 in supporting information). The ¹H NMR spectrum of **1** exhibits peaks at δ values of 8.06 (H₆), 7.41 (H₄), 6.63 (H₅) and 6.49 (H₃) ppm assigned to the protons of the pyridine ring. In addition, the protons of the aliphatic chain are also observed and assigned easily, with the H₇, H₉ and H₁₀ and OH protons appearing as a broad multiplet in the 3.34–3.49 ppm range while the remaining signals are observed at δ values of 4.20 (H₈), 1.68 (H₁₁) and 0.66 (H₁₂) ppm. Finally, the protons of the Si(OCH₃)₃ group are observed as a neat singlet at 3.56 ppm and that of NH is observed at 3.90 ppm. The ¹³C NMR spectrum evidenced all the carbon nuclei of the ligand confirming the structure of **1** (Table S1).

3.2. Synthesis of metal containing materials

Two batches of pure siliceous MCM-41 (hereafter denoted as MCM) **2** and **2*** (* denotes a different batch) were obtained by

Scheme 1. Preparation of glypy ligand (**1**).

a template approach, adopting a synthetic procedure described previously [43]. From the two MCM batches one was used to prepare Mo^{II} containing materials while the remaining (denoted with an *) was used to prepare the Mo^{VI} counterparts, according to Scheme 2.

Afterwards the silica-matrix mesoporous host material was derivatized by grafting ligand **1**, yielding MCM-glypy (**3**, **3***) [53]. Treatment of MCM-glypy (**3**, **3***) with a dichloromethane solution of the molybdenum complexes [Mo₂(CO)₃(NCMe)₂] or [MoO₂Cl₂(thf)₂] led to new metal containing materials, MCM-glypy-Mo^{II} (**4**) and MCM-glypy-Mo^{VI} (**5**). Elemental analyses revealed a 1.80 wt% Mo (0.19 mmol g⁻¹) content for material **4** and 4.62 wt% Mo (0.48 mmol g⁻¹) for material **5**. The synthetic pathway adopted is outlined in Scheme 2. All materials were conveniently characterized by DRIFT, powder XRD and ²⁹Si and ¹³C CP MAS SS-NMR. Sorption/desorption N₂ isotherms were also carried out for textural parameters estimation. All spectroscopic/textural characterization features discussed in the following lines were found to be in agreement with related hybrid matrix mesoporous materials recently reported by us using the same ligand [54].

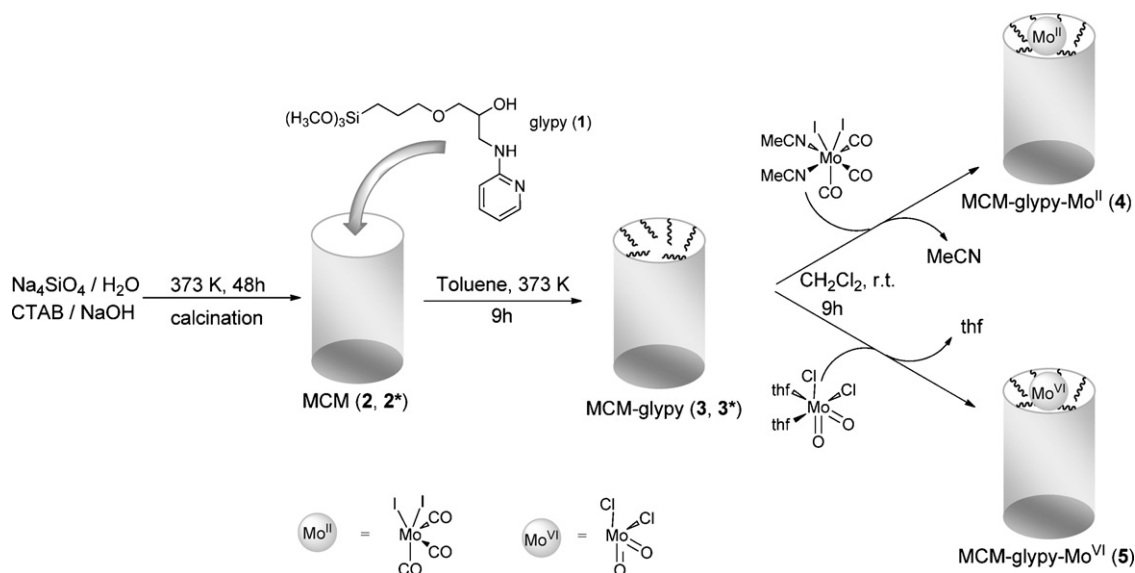
The FTIR spectra of the grafted materials are presented in Fig. 1. The DRIFT spectrum of the MCM host material is typical of a silicate evidencing a broad band in the 3600–2600 cm⁻¹ range due to hydrogen bonding silanol groups. A sharp band at 3754 cm⁻¹ is due to silanol groups not involved in hydrogen bonding. Other important features comprise the band at ca. 1640 cm⁻¹ due to δOH bending modes while the intense broad band at 1260–900 cm⁻¹ is assigned to the asymmetric stretching vibration modes of the

mesoporous framework (νSi–O–Si). After grafting of ligand **1**, which affords the material MCM-glypy (**3**, **3***), the DRIFT spectrum shows an overall similar profile dominated by the absorptions of the host MCM material. Additionally new bands were detected evidencing the ligand presence within the pores. These 2940 and 2870 cm⁻¹ bands can be assigned to the νCH stretching modes of the aliphatic chain in **1**. At the same time the 1628 and 1654 cm⁻¹ bands can be related with the νC=C and νC=N modes. In addition the bands at 1450 and 1590 cm⁻¹ are due to the βCH in-plane bending modes of the organic moieties.

After binding the molybdenum complexes [Mo₂(CO)₃(NCMe)₂] and [MoO₂Cl₂(thf)₂], which afford materials MCM-glypy-Mo^{II} (**4**) MCM-glypy-Mo^{VI} (**5**), respectively, several changes/additional bands in the corresponding DRIFT spectra are detected.

In what concerns material **4** the most remarkable feature is the observation of three bands at 1880, 1960 and 2030 cm⁻¹ assigned to the νC≡O modes. These bands are inclusively shifted relatively to the [Mo₂(CO)₃(NCMe)₂] precursor complex. This is indicative of the metal–ligand binding. Additionally, the bands due to the νC≡N vibrational modes from the CH₃CN ligands are not found, indicating that such ligands have been replaced by the immobilized ligand. The most relevant spectral feature for the MCM-glypy-Mo^{VI} (**5**) material is a pair of bands observed at 958 and 939 cm⁻¹ assigned to the ν_{sym}Mo=O modes of the [MoO₂Cl₂] core.

Fig. 2 shows the X-ray diffraction powder patterns of materials **2–4**. The calcined material MCM (**2**) powder pattern clearly shows four reflections in the 2–10° 2θ range. The peaks are indexed to a hexagonal cell as (100), (110), (200) and (210). From the (100)

Scheme 2. Preparation of derivatized mesoporous materials with Mo^{II} and Mo^{VI} species.

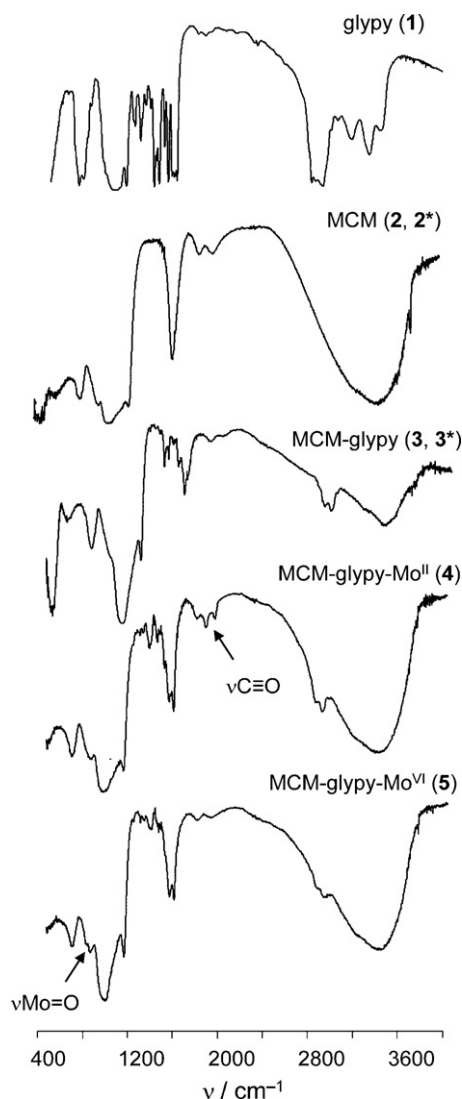


Fig. 1. Infrared spectra of glypy (1), MCM (2, 2*), MCM-glypy (3, 3*), MCM-glypy-Mo^{II} (4) and MCM-glypy-Mo^{VI} (5).

reflection the d_{100} value is estimated to be 36.8 Å, corresponding to a lattice constant of $a = 42.4$ Å ($a = 2d_{100}/\sqrt{3}$).

Materials 3 and 4, obtained after subsequent stepwise functionalization with 1 and Mo^{II}, still show three reflections although with

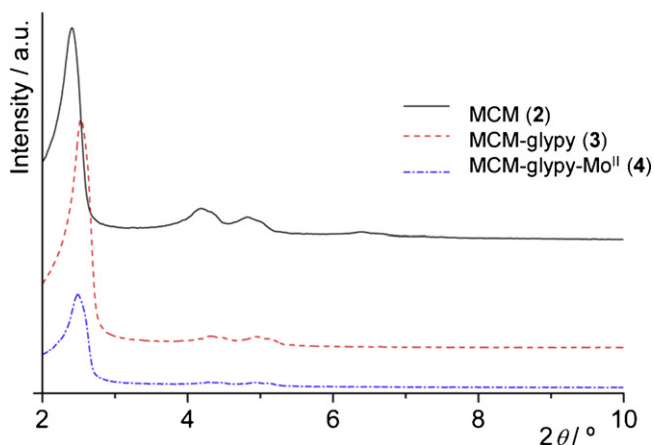


Fig. 2. XRD powder patterns of MCM (2), MCM-glypy (3), MCM-glypy-Mo^{II} (4).

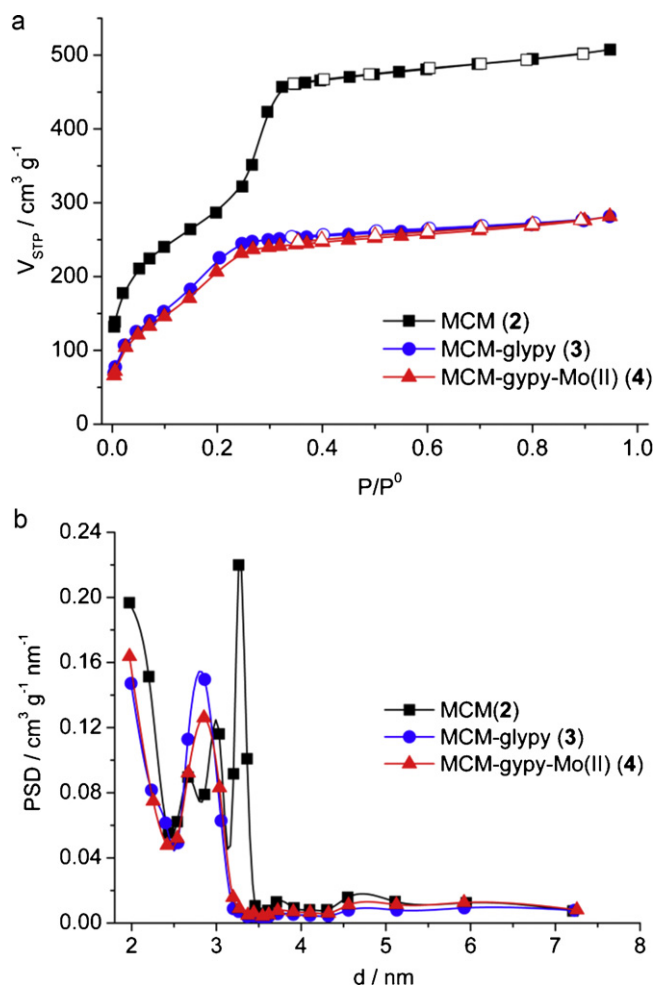


Fig. 3. (a) Nitrogen sorption isotherms and (b) pore size distribution curves at 77 K for MCM (2), MCM-glypy (3) and MCM-glypy-Mo^{II} (4) materials.

a slight deviation of the position maxima towards higher 2θ values as compared to 2. For MCM-glypy (3) material the d_{100} value is 34.8 Å with a corresponding lattice constant of $a = 40.2$ Å; for MCM-glypy-Mo^{II} (4) the values are respectively $d_{100} = 35.5$ Å and $a = 41.0$ Å.

Similar observations were made for the set of materials 2*, 3* and 5 used for the Mo^{VI} derivatives (denoted with an * since the parent MCM is from a different batch). All data is collected in Table 1, summarizing the relevant textural properties of all materials leading to the preparation of both Mo^{II} and Mo^{VI} derivatives.

The observed peaks intensity reduction is common to all materials; it is even more significant in the materials with the Mo cores. This is not due to a crystallinity loss, but rather to an X-ray scattering contrast reduction between the silica walls and pore-filling material. This has been observed for other types of materials and is well described in the literature [55–57].

Nitrogen sorption/desorption studies at 77 K were performed and have revealed that pristine MCM sample exhibits a reversible type IV isotherm (Fig. 3a), typical of mesoporous solids (pore width between 2 nm and 50 nm, according to IUPAC) [57]. The calculated textural parameters (S_{BET} and V_p) of these materials (Table 1) agree with literature data [58,59]. The capillary condensation/evaporation step in pristine MCM sample appears in the 0.24–0.34 relative pressures range while the sharpness of this step reflects a uniform pore size distribution.

Table 1Textural parameters of host and composite materials, from powder XRD and N₂ isotherms at 77 K.

Material	d_{100} (Å)	a (Å)	S_{BET} (m ² g ^{−1})	ΔS_{BET}^a (%)	V_p (cm ³ g ^{−1})	ΔV_p^b (%)	d_p (nm)
MCM(2)	36.8	42.4	1037	–	0.78	–	3.2
MCM-glypy (3)	34.8	40.2	764	−26	0.43	−45	2.8
MCM-glypy-Mo ^{II} (4)	35.4	40.8	714	−31	0.43	−44	2.8
MCM(2*)	34.9	40.2	1027	–	0.82	–	3.2
MCM-glypy (3*)	35.4	40.8	1063	3.5	0.75	−8.5	3.0
MCM-glypy-Mo ^{VI} (5)	36.4	42.0	989	−3.7	0.68	−17	3.0

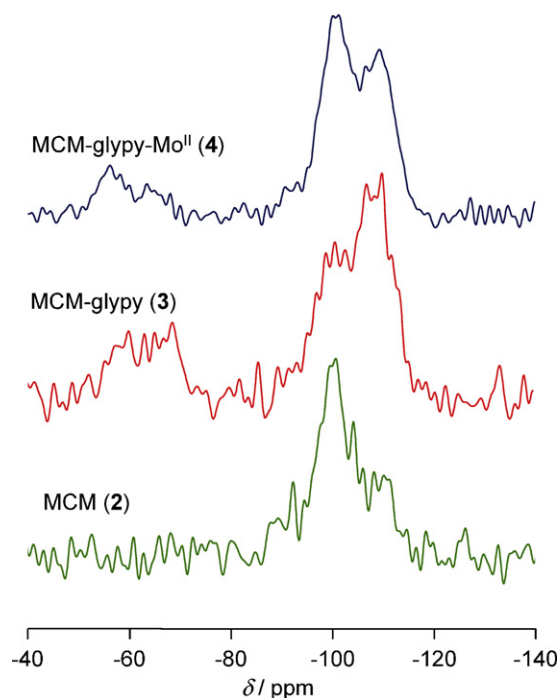
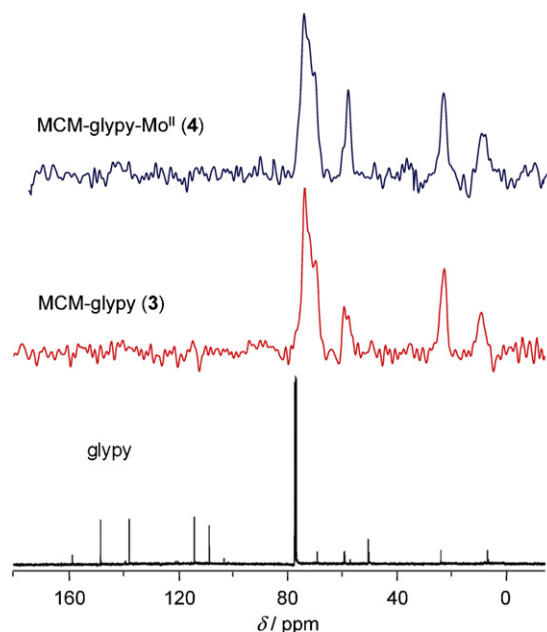
^a Surface area variation relatively to parent MCM.^b Total pore volume variation relatively to parent MCM.

The functionalized material MCM-glypy (3) isotherm revealed much lower N₂ uptake, accounting for the decreases in both S_{BET} (26%) and V_p (45%). These findings indicate that the ligand immobilization on the internal silica surface was accomplished (Fig. 3, Table 1).

For the MCM-glypy-Mo^{II} (4) material, the S_{BET} and V_p relative decrease related to MCM is 31% and 44%, respectively. This result is in agreement with the P/P^0 coordinates decrease on the isotherms inflection points after post-synthesis treatments [60]. The capillary condensation step height, which is related to the volume of pore space confined by adsorbate film on the pore walls, is smaller in the case of the modified MCM-glypy (3) material. Furthermore, the maximum of the PSD curve (Fig. 3b) determined by the BJH method, d_{BJH} , for MCM material decreases from 3.2 nm to less than 3 nm (Table 1). For the MCM-glypy-Mo^{VI} (5) material, the relative decrease in S_{BET} and V_p when compared to MCM is 4% and 17%, respectively. These decreases are less expressive than in the other set of materials.

All materials were also characterized by ¹³C CP MAS and ²⁹Si CP MAS SS-NMR. Fig. 4 shows the ²⁹Si CP MAS spectra for pristine calcined MCM, along with the derivatized materials MCM-glypy (3) and MCM-glypy-Mo^{II} (4).

Unmodified MCM displays two broad convoluted resonances in the ²⁹Si CP MAS NMR spectrum at −110 and −100 ppm,

**Fig. 4.** ²⁹Si CP MAS SS-NMR spectra for MCM (2), MCM-glypy (3) and MCM-glypy-Mo^{II} (4) materials.**Fig. 5.** ¹³C CP MAS SS-NMR spectra for MCM-glypy (3) and MCM-glypy-Mo^{II} (4) materials. ¹³C solution NMR spectrum of glypy is also shown for comparison.

assigned to Q⁴ and Q³ species of the silica framework, respectively [$Q^n = \text{Si}(\text{OSi})_n(\text{OH})_{4-n}$]. A weak shoulder is also observed at −90 ppm due to the Q² species. The Q³ sites are associated with single silanols Si–OH (including hydrogen-bonded silanols), whereas the Q² sites correspond to geminal silanols (Si(OH)₂). The ²⁹Si CP MAS spectrum of MCM-glypy (3) also displays three broad signals at −50, −57 and −67 ppm, assigned to T¹, T² and T³ organosilicon species, respectively [$T^m = \text{RSi}(\text{OSi})_m(\text{OMe})_{3-m}$]. As expected the subsequent reaction of MCM-glypy (3) material with the [MoL₂(CO)₃(NCMe)₂] organometallic complex does not significantly change the ²⁹Si CP MAS NMR spectra. Comparing the three materials prepared by this approach, the *in situ* grafting of ligand 1 in MCM (2) affording MCM-glypy (3) results in the reduction of the Q² and Q³ resonances. A concomitant increase of the Q⁴ resonance compared to the parent mesoporous MCM material 2, indicating the successful ligand grafting, can also be observed. This trend persists after the derivatized material MCM-glypy-Mo^{II} (4) synthesis. This behavior is consistent with an esterification of isolated silanol groups (single and geminal) by nucleophilic substitution at the silicon atom in the organic ligand.

The ¹³C CP MAS SS-NMR spectra (Fig. 5) of the MCM-glypy (3) and MCM-glypy-Mo^{II} (4) materials are quite similar to those of the ligand glypy (1), confirming the binding of the ligand to the surface.

The SS-NMR studies for the Mo^{VI} route – materials 2*, 3* and 5 – led to identical conclusions established for 2–4 composite

materials; a full description of spectral data can be found in Section 2.

3.3. Photocatalytic degradation studies

The photocatalytic activity of the prepared derivatized materials was evaluated on an organic dye photodegradation reaction. In the present study rhodamine B (rhB) was used as the model pollutant molecule. Control experiments of rhB direct photolysis (without catalyst) and in the presence of pristine MCM (2) were also performed for 2 h.

Since photo-oxidation usually takes place at the catalyst surface, the adsorption characteristics of the photocatalyst/pollutant system are considered important parameters on a photocatalytic study. Considering this, before the photocatalytic experiments, adsorption studies have been carried out in order to check rhB ability to be adsorbed on the different materials surface. During these experiments, performed under dark conditions, a strong decrease on rhB concentration in solution was observed for all the materials tested. The time required to ensure optimum adsorption–desorption equilibrium was found to be 2 h.

After this period all solids were dark pink in color and the solution was found to be strongly discolored. The decrease in dye concentration was 98.3% for 5, 94.4% for pristine MCM (2) and 93.8% for 4. At first glance and considering these results, an adsorption process of rhB onto these derivatized materials can be suggested as an efficient method for rhB solutions decolorization, without any special equipment requirements. Fig. 6 presents the chronological evolution of both the solution and catalyst color for the particular case of MCM (2).

In the case of the solutions it is easily observed the strong decolorization of the solutions (from the –2 h to 0 h in the sorption period). As for the powder it is possible to verify that rhB is adsorbed at the start of the photocatalytic process and at the end is strongly decolorized showing only a very light yellow color evidencing the clear photodecolorization of the adsorbed dye.

Fig. 7 shows the absorption spectra of the different systems studied during the photo-irradiation period (the adsorption occurrence was not considered for range reasons).

The absorption spectra during the direct photolysis time clearly show a decrease in all the characteristic rhB absorption bands (Fig. 7a). A different and more complex behavior was observed for all the catalytic materials tested. However it must be noted that in all the photo-catalyzed systems a decrease on the 554 nm band with time, was visualized. This absorbance intensity decrease is accompanied by a concomitant blue-shift of the band (hypsochromic). This phenomenon is due to the appearance of degradation products formed by the loss of one or more ethyl groups of the original substrate. A similar situation has already been described in the literature [61]. Wavelengths lower than 554 nm observed in the absorption spectra suggest the presence of different degradation products depending on the catalytic system used.

It must be stated that after the photo-irradiation period all catalysts were white in color (no dye remaining adsorbed). In face of these results it can be concluded that the complete decolorization of rhB aqueous solutions and the simultaneous materials recovery were reached. In addition we have also conducted powder XRD measurements on the powders after irradiation. The diffraction patterns (not shown) were found to be unaffected by the photocatalytic conditions thus evidencing the stability of the materials under such high energetic conditions.

In addition another point is worth mentioning. According to Fig. 7, degradation of rhB in the presence of Mo containing catalysts is somewhat slower than in the direct photolysis or using MCM (2). A possible cause for such happening is that the Mo species are probably quenching rhB excited state leading to dye degradation

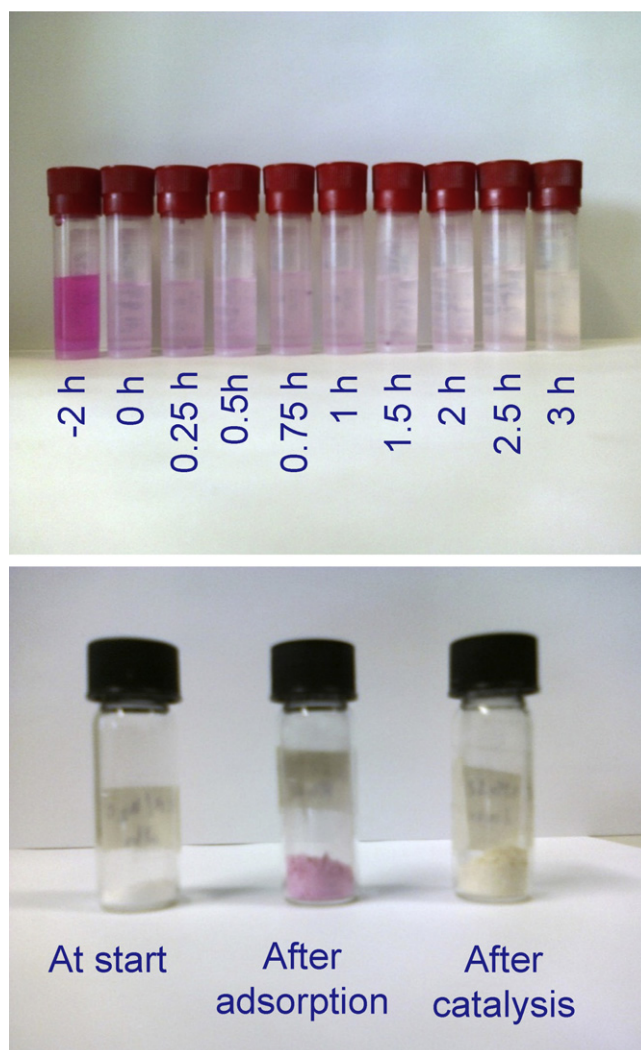


Fig. 6. Photographs of the solutions and of the MCM (2) powder catalyst before, during and after photocatalytic experiment. In the solutions the intense pink solution is the 20 ppm original rhB solution (marked with –2 h), while the solution referenced with “0 h” represents the time when the irradiation is started. (For interpretation of the references to color in this figure legend, the reader is referred to the web version of the article.)

arising not from primary photochemistry but from secondary processes. This will be addressed later in this paper.

3.4. By-products identification

Considering the results obtained by the UV–vis spectra qualitative analysis, and with the purpose to understand the mechanistic differences between these catalysts an ESI-MS study towards identification of intermediates was performed.

In order to identify and quantify the compounds formed during the rhB photocatalytic degradation process, ESI-MS measurements from the reaction solutions, have been performed. Fig. 8 shows the temporal evolution of rhB dye concentration during the degradation processes, in terms of abundance.

From Fig. 8, ESI-MS results show that rhB degradation kinetics is in fact slower in the presence of Mo catalysts, thus corroborating with UV–vis data, as described above.

In addition MS spectra were used to identify the species in solution that were produced during the catalytic process as reported previously by others [62]. From all the photodegradation experiments performed the direct photolysis was the only one originating

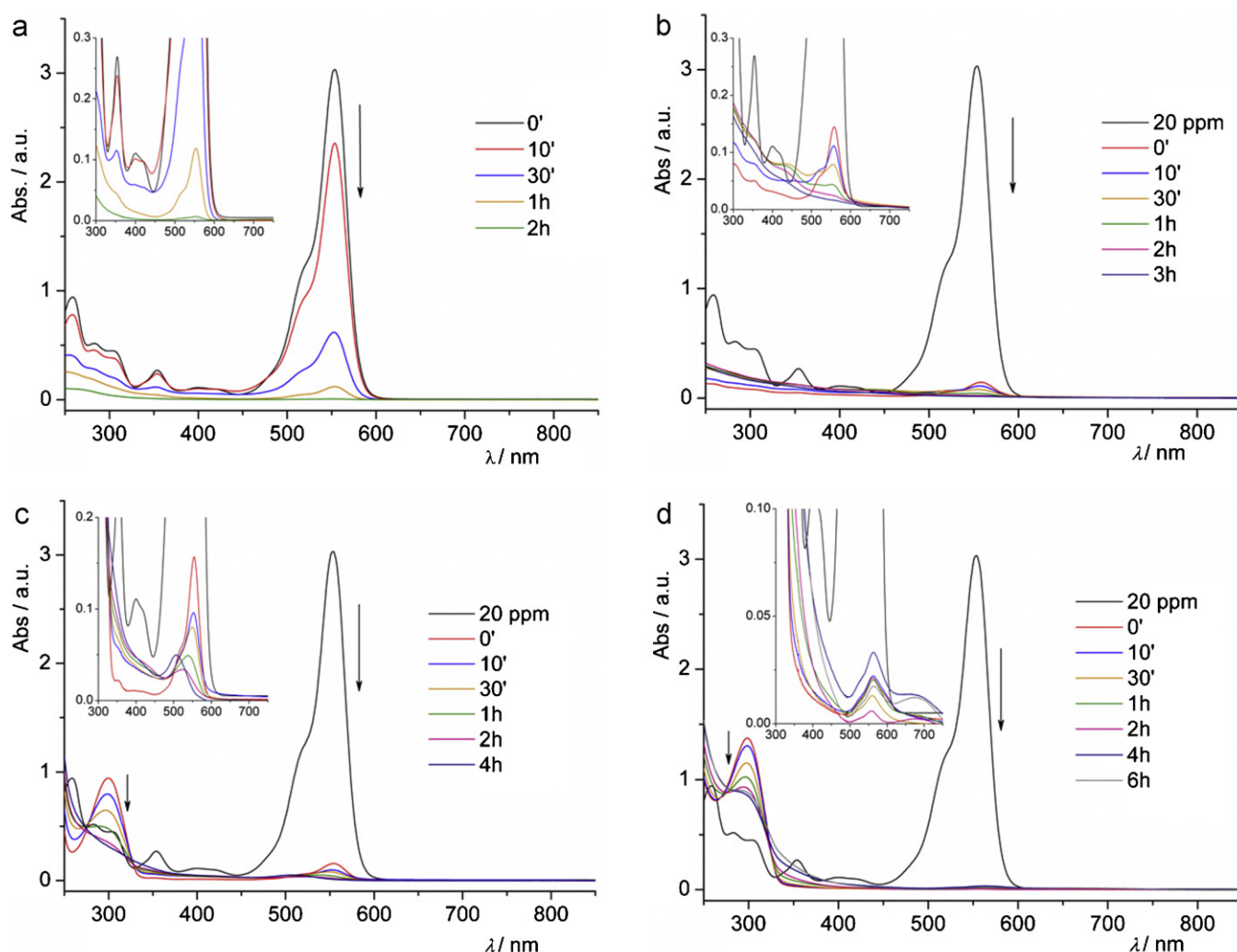


Fig. 7. Time-dependent absorption spectra of 150 mL of a 20 ppm rhB photo-irradiated solution: (a) direct photolysis and in the presence of 150 mg of (b) MCM (2), (c) MCM-glypy-Mo^{II} (4) and (d) MCM-glypy-Mo^{VI} (5). The arrow indicates direction with increasing time.

three products. These three products were identified as rhB-C₂H₄ and rhB-CO₂, the latter further yielding rhB-(C₂H₄)₂-CO₂ (see Scheme 3 for details). It is interesting to note that direct loss of CO₂ was found to occur only in the direct photolysis process. In

all the other catalytic processes CO₂ loss was detected at more advanced stages of the degradation process. For instance, in the presence of MCM (2) degradation of rhB led to loss of ethyl groups and only afterwards there was loss of CO₂. At the end of this catalytic degradation experiment the major product detected was the xanthene moiety, after consecutive loss of all ethyl groups and of the benzoate group.

When the degradation was performed using either the Mo^{II} or Mo^{VI} containing catalysts, some intermediates were found to be similar (namely some de-ethyl degradates, according to Scheme 3). However at the end of the reactions, it was found that the major product using material 4 as photocatalyst was aniline; in the presence of photocatalyst 5 a set of small compounds was detected (Scheme 3) – aniline and hydroxyl aniline; benzoic and hydroxybenzoic acids; dihydropyran. Most probably H₂O and CO₂ have also been formed but cannot be probed with this MS approach. These achievements agree with previous published results concerning rhB photodegradation using TiO₂ catalysts [63].

It should be mentioned that from the ESI-MS data no Mo species were detected in any of the analyzed solutions. This fact is quite relevant accounting for the robustness of the Mo containing catalysts to leaching during the photocatalytic process. This results in a true heterogeneous catalytic process.

Also is important to notice that all photocatalytic experiments were conducted under normal atmosphere, which is, using as a

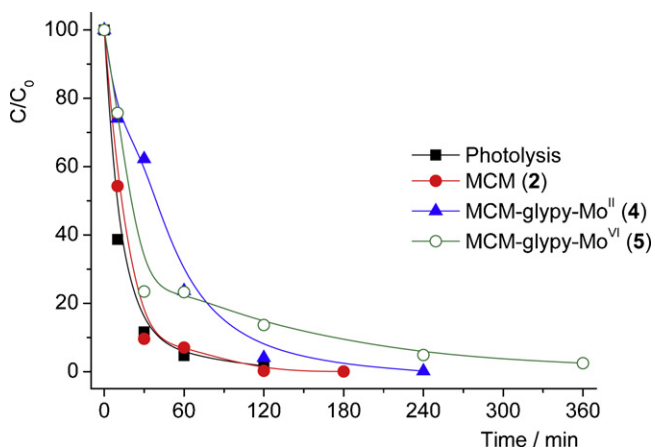
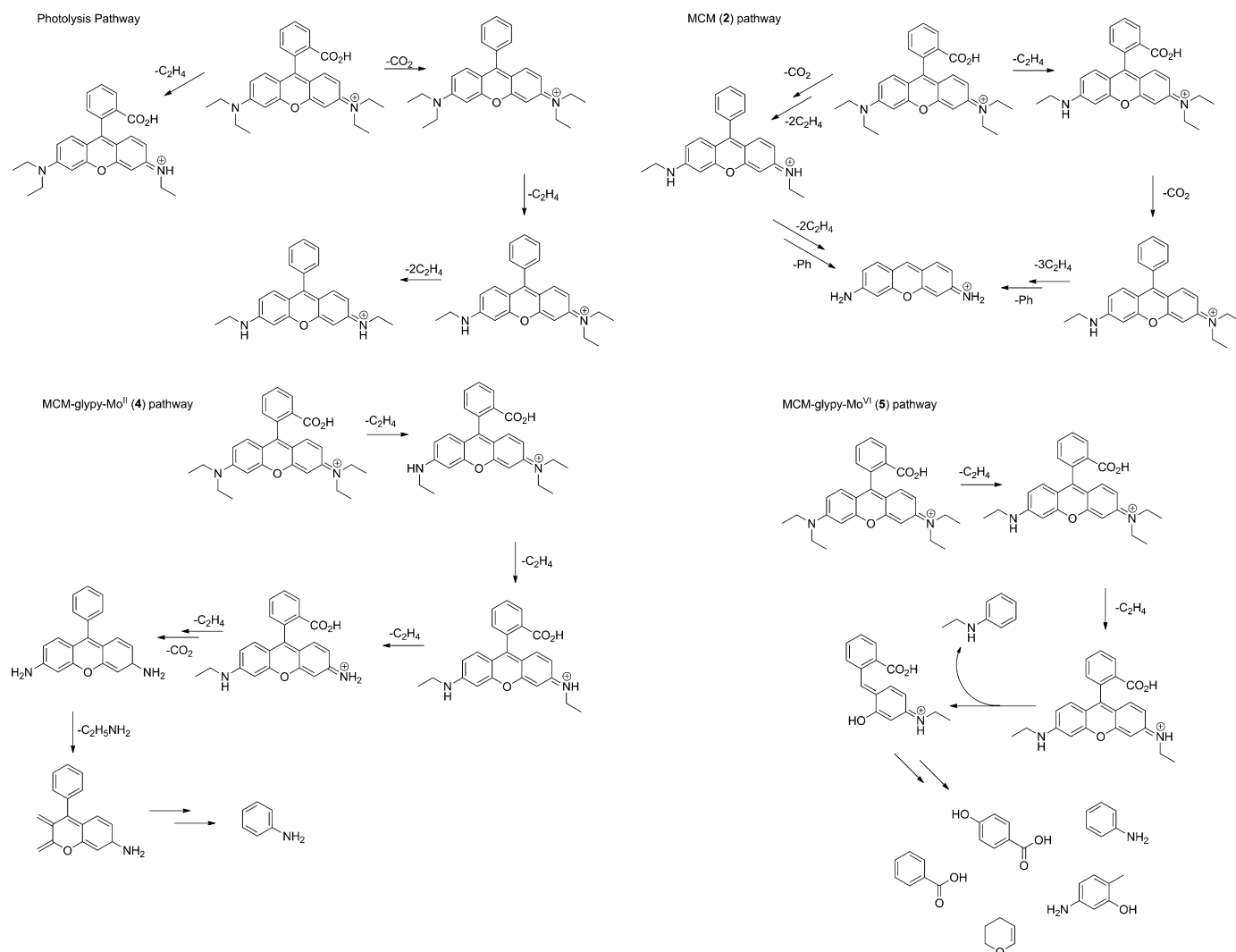


Fig. 8. Time-dependent evolution of the main species detected by mass spectrometry of 150 mL of a 20 ppm rhB photo-irradiated solution: (a) direct photolysis and in the presence of 150 mg of (b) MCM (2), (c) MCM-glypy-Mo^{II} (4) and (d) MCM-glypy-Mo^{VI} (5). Lines are eye guide only.



Scheme 3. Degradation pathways of rhB under the different conditions reported.

possible oxidant O_2 from air, without the addition of other oxidants. This fact is very important, because as in other studies the photodegradation is carried out with the addition of H_2O_2 . Thus it demonstrates the effectiveness of materials with Mo during photodegradation without addition of oxidants, leading to the conclusion that it is an environmentally friendly process, with atom economy and in terms of process becomes less expensive. Compared to previous reports on rhB degradation [61,64], the present work deals with the successful degradation of a somewhat concentrated solution (20 ppm). The results show that higher degradation rates are attained compared to the literature reports.

Concerning the question of whether rhB photodegradation arises from either primary or secondary photochemistry in the presence of Mo species we conducted a control experiment. This experiment was performed using direct photolysis during 2 h and afterwards adding material **5** as photocatalyst and irradiating the mixture again. As expected, it was found that during the first irradiation period the same three products were present (Scheme 3, photolysis pathway). After addition of the Mo photocatalyst **5**, ESI-MS analysis of the solution at the end of the reaction revealed the existence of the degradation products similar to those described above for the catalyzed process using photocatalyst **5** (Scheme 3, MCM-glypy-Mo^{VI} pathway). From this result it is clear that formation of such small weight compounds may be due to secondary photochemistry arising

from the presence of Mo photocatalysts, acting not only directly on rhB degradation process, but also on the direct photolysis intermediates (mainly rhB- C_2H_4 and rhB- CO_2). In addition, some of the detected degradates from these Mo-pathways include aniline and benzoic acid, which may be regarded as industrially relevant starting materials. For instance aniline is a precursor of methylene diphenyldiisocyanate (a precursor of polyurethanes) and benzoic acid is used as a food preservative.

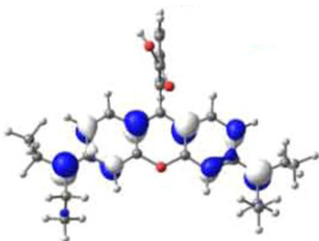
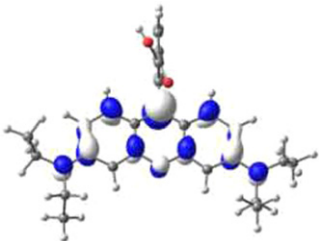
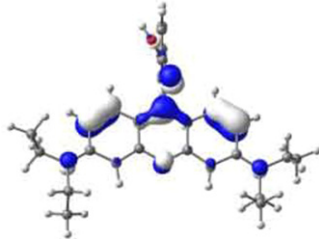
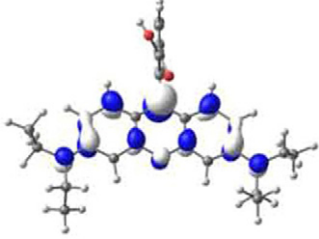
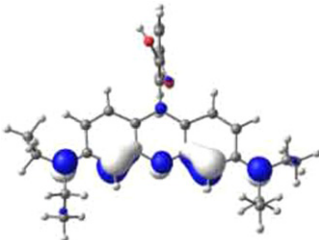
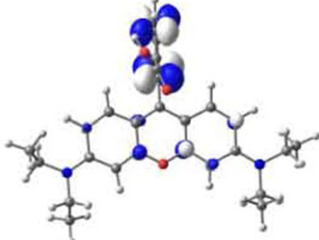
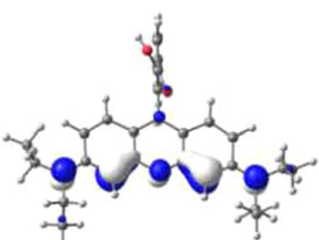
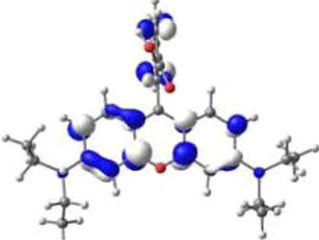
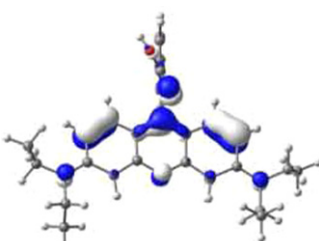
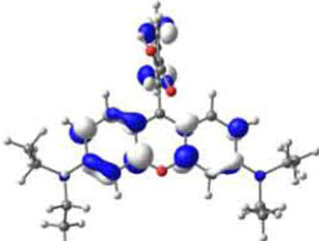
3.5. TD-DFT analysis

To understand some features of the photodegradation studies, time-dependent density functional theory (TD-DFT) calculations on rhB have also been conducted. The calculations were performed at the B3LYP/6-311g** level of theory as implemented in the G03 package and the 40 lowest singlet-singlet transitions were predicted. The output of the TD-DFT calculation shows a good agreement with the experimental electronic spectrum (Fig. 9). The assignments of the most important transitions, that are the most representative of the experimental spectrum, were performed and are summarized in Table 2 along with representation of the involved orbitals in the transitions.

Based on the predicted transitions it is possible to see intramolecular charge transfer within xanthene itself or from this to benzoate moiety. This is also in agreement with the results from

Table 2

Highest energy singlet–singlet transitions and orbital contours obtained from TD-DFT calculation at the B3LYP/6-311G** level of theory.

Excitation	Composition ^a	Starting orbital	Ending orbital	<i>E</i> (eV)	λ (nm)	λ_{max}^b (nm)	OS ^c ($\times 10^2$)
1	H \rightarrow L (75%)			2.72	456	553	86.7
2	H – 2 \rightarrow L (65%)			3.73	332	354	10.2
3	H – 1 \rightarrow L + 2 (83%)			4.93	251	306	25.6
4	H – 1 \rightarrow L + 3 (80%)			5.16	240	258	24.0
5	H – 2 \rightarrow L + 3 (73%)			5.76	215	–	38.0

^a H: HOMO, L: LUMO.^b Experimental UV–vis values.^c Oscillator strength.

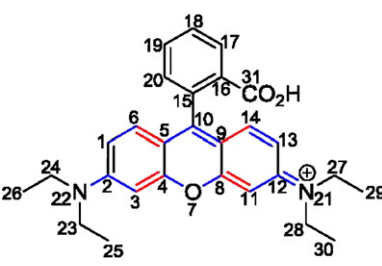
NBO analyses where the Wiberg bond orders change quite a bit for selected bonds (Table 3).

The orbital contours of the starting and ending orbitals for the given transitions are shown in Table 2. The orbital character is mainly bonding, resulting in a strengthening of the bonds in the excited state compared to the fundamental state. This is confirmed by an increase of the Wiberg bond orders obtained from NBO analyses, according to Table 3.

Assuming this analysis to have responsibility in the primary photochemistry of rhB it may explain the fact that rhB

photodegradation, by direct photolysis leads mainly to de-ethylation and/or decarboxylation products, as observed here and previously reported by others [61]. However, to explain the extended degradation detected when using the Mo-containing heterogeneous catalysts it seems plausible to assume that Mo centers are acting as quenchers of rhB excited state which enables the secondary photochemistry leading to the observed products, as described earlier in this work. This is supported by literature reports on the photocatalytic activity of Mo catalysts [36–40].

Table 3
Wiberg bond orders of singlet (S), triplet (T) states and respective variation obtained from NBO analysis. The colored bonds represent the weakened (blue) and strengthened (red) ones.

Numbering scheme	Bond	Wiberg BO		
		S	T	Δ
	C ₁ –C ₆	1.610	1.550	–0.060
	C ₂ –C ₃	1.286	1.245	–0.041
	C ₂ –N ₂₂	1.251	1.222	–0.029
	C ₃ –C ₄	1.455	1.480	0.025
	C ₄ –O ₇	1.002	0.974	–0.028
	C ₅ –C ₆	1.213	1.233	0.020
	C ₅ –C ₁₀	1.307	1.236	–0.071
	O ₇ –C ₈	1.000	0.973	–0.027
	C ₈ –C ₁₁	1.456	1.480	0.024
	C ₉ –C ₁₀	1.312	1.229	–0.083
	C ₉ –C ₁₄	1.210	1.232	0.022
	C ₁₁ –C ₁₂	1.285	1.243	–0.042
	C ₁₂ –N ₂₁	1.252	1.223	–0.029
	C ₁₃ –C ₁₄	1.613	1.552	–0.061

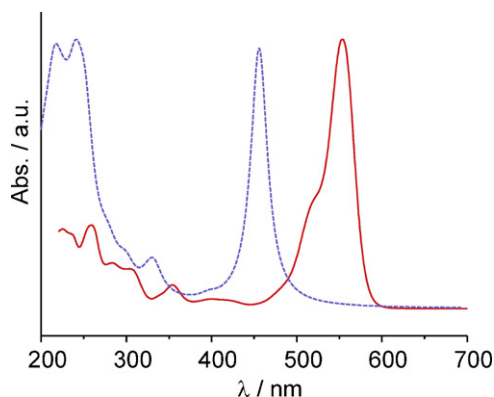


Fig. 9. Experimental (—) and TD-DFT calculated at the B3LYP/6-311G** level (....) UV-vis spectra of rhB.

4. Conclusions

The present work evidences the tunable features of a given heterogeneous catalyst towards the photodegradation of a model dye. The MCM-41 silica support has revealed some catalytic activity in the process. Despite this, the use of immobilized Mo^{II} or Mo^{VI} species at the surface of MCM definitely contributed to further degradation of the dye for which the metal species cannot be innocent nor its oxidation state. In fact these have been found to trigger secondary photochemical processes most probably by quenching rhB excited state thus allowing extended degradation of the dye. Additionally, all materials showed stability under photodegradation conditions as evidenced by powder XRD measurements before and after the process.

Additionally, the catalytic process was carried out exclusively under aerobic conditions, i.e., in the absence of any external oxygen source other than air. This is an advantage over several other catalytic processes since the addition of an oxygen source such as H₂O₂, organic hydroperoxides or even “pure” O₂ is common.

Based on previous reports, it is described that degradation of rhB under such conditions occurs mainly via de-ethylation. However when photolysis is promoted in the presence of MCM or Mo containing materials other products are formed leading to degradation of the xanthene and benzoate moieties.

DFT theoretical calculation explain why direct photolysis leads only to de-ethylation and/or decarboxylation by showing that charge transfer transitions will localize mainly in those moieties resulting in a predicted variation of bond orders. This seems to be circumvented by the use of catalytically active Mo species which

lead to further degradation of those strengthened moieties most probably by quenching the excited state of rhB. Among degradates it is also possible to find aniline (used for preparing polyurethane precursors) and benzoic acid (used as food preservative) which have industrial relevance. In this way it is shown in this work that degradation of a dye (rhB) can yield relevant industrial building blocks/additives.

Acknowledgements

The authors thank FCT, POCI and FEDER (project POCI/QUI/71576/2006) for financial support.

Appendix A. Supplementary data

Supplementary data associated with this article can be found, in the online version, at [doi:10.1016/j.apcatb.2011.11.036](https://doi.org/10.1016/j.apcatb.2011.11.036).

References

- [1] C.T. Kresge, M.E. Leonowicz, W.J. Roth, J.C. Vartuli, J.S. Beck, *Nature* 359 (1992) 710–712.
- [2] K. Moller, T. Bein, *Chem. Mater.* 10 (1998) 2950–2963.
- [3] D. Zhao, P. Yang, Q. Huo, B.F. Chmelka, G.D. Stucky, *Curr. Opin. Solid State Mater. Chem.* 3 (1998) 111–115.
- [4] P. Yang, D. Zhao, B.F. Chmelka, G.D. Stucky, *Chem. Mater.* 10 (1998) 2033–2036.
- [5] F. Rambaud, K. Valle, S. Thibaud, B. Julian-Lopez, C. Sanchez, *Adv. Funct. Mater.* 19 (2009) 2896–2905.
- [6] C.D. Nunes, P.D. Vaz, A.C. Fernandes, P. Ferreira, C.C. Romão, M.J. Calhorda, *Eur. J. Pharm. Biopharm.* 66 (2007) 357–365.
- [7] D.M. Ford, E.E. Simanek, D.F. Shantz, *Nanotechnology* 16 (2005) S458–S475.
- [8] A. Chenite, Y.L. Page, A. Sayari, *Chem. Mater.* 7 (1995) 1015–1019.
- [9] Z. Luan, C.F. Cheng, W. Zhou, J. Klinowski, *J. Phys. Chem.* 99 (1995) 1018–1024.
- [10] P.T. Tanev, M. Chibwe, T.J. Pinnavaia, *Nature* 368 (1994) 321–323.
- [11] M.S. Morey, G.D. Stucky, S. Schwarz, M. Fröba, *J. Phys. Chem. B* 103 (1999) 2037–2041.
- [12] A.B. Bourlino, M.A. Karakassides, D. Petridis, *J. Phys. Chem. B* 104 (2000) 4375–4380.
- [13] P.D. Vaz, C.D. Nunes, M. Vasconcellos-Dias, M.M. Nolasco, P.J.A. Ribeiro-Claro, M.J. Calhorda, *Chem. Eur. J* 13 (2007) 7874–7882.
- [14] T.A. Fernandes, C.D. Nunes, P.D. Vaz, M.J. Calhorda, P. Brandão, J. Rocha, I.S. Gonçalves, A.A. Valente, L.P. Ferreira, M. Godinho, P. Ferreira, *Microporous Mesoporous Mater.* 112 (2008) 14–25.
- [15] M. Vasconcellos-Dias, C.D. Nunes, P.D. Vaz, P. Ferreira, P. Brandão, V. Félix, M.J. Calhorda, *J. Catal.* 256 (2008) 301–311.
- [16] V.M. Correia, T. Stephenson, S. Judd, *J. Environ. Technol.* 15 (1994) 917–929.
- [17] I.I. Raffainer, P.R. Rohr, *Ind. Eng. Chem. Res.* 40 (2001) 1083–1089.
- [18] N.L. Stock, J. Peller, K. Vinodgopal, P.V. Kamat, *Environ. Sci. Technol.* 34 (2000) 1747–1750.
- [19] X. Tao, W. Ma, T. Zhang, J. Zhao, *Angew. Chem. Int. Ed.* 40 (2001) 3014–3016.
- [20] W. Ma, J. Li, X. Tao, J. He, Y. Xu, J.C. Yu, J. Zhao, *Angew. Chem. Int. Ed.* 42 (2003) 1029–1032.
- [21] S. Zhu, T. Xu, H. Fu, J. Zhao, Y. Zhu, *Environ. Sci. Technol.* 41 (2007) 6234–6239.
- [22] H.J.H. Fenton, *J. Chem. Soc.* 6 (1894) 899–911.

- [23] B. Ensing, F. Buda, P. Blochl, J.E. Baerends, *Angew. Chem. Int. Ed.* 40 (2001) 2893–2895.
- [24] J. Ma, W. Song, C. Chen, W. Ma, J. Zhao, Y. Tang, *Environ. Sci. Technol.* 39 (2005) 5810–5815.
- [25] S.S. Gupta, M. Stadler, C.A. Noser, A. Chosh, B. Steinhoff, D. Lenoir, C.P. Horwitz, K.-W. Schramm, T.J. Collins, *Science* 296 (2002) 326–328.
- [26] N. Chahbane, D.-L. Popescu, D.A. Mitchell, A. Chanda, D. Lenoir, A.D. Ryabov, K.-W. Schramm, T.J. Collins, *Green Chem.* 9 (2007) 49–57.
- [27] N. Chahbane, D. Lenoir, S. Souabi, T.J. Collins, K.-W. Schramm, *Clean* 35 (2007) 459–464.
- [28] T.J. Collins, *Acc. Chem. Res.* 35 (2002) 782–790.
- [29] S.R. Segal, S.L. Suib, L. Foland, *Chem. Mater.* 9 (1997) 2526–2532.
- [30] O.C. Monteiro, M.H.M. Mendonca, M.I.S. Pereira, J.M.F. Nogueira, *J. Solid State Electrochem.* 10 (2006) 41–47.
- [31] R. Albuquerque, M.C. Neves, M.H. Mendonca, T. Trindade, O.C. Monteiro, *Colloids Surf. A: Physicochem. Eng. Aspects* 328 (2008) 107–113.
- [32] A. Franco, M.C. Neves, M.L.R. Carrott, M.H. Mendonca, M.I. Pereira, O.C. Monteiro, *J. Hazard. Mater.* 161 (2009) 545–550.
- [33] M.C. Neves, J.M.F. Nogueira, T. Trindade, M.H. Mendonca, M.I. Pereira, O.C. Monteiro, *J. Photochem. Photobiol. A: Chem.* 204 (2009) 168–173.
- [34] O.C. Monteiro, R. Marques, M.D. Carvalho, *Mater. Chem. Phys.* 119 (2010) 418–423.
- [35] W. Lee, Y.R. Do, K. Dwight, A. Would, *Mater. Res. Bull.* 28 (1993) 1127–1134.
- [36] C.A. Paez, N.J. Castellanos, F.O. Martinez, F. Ziarelli, G. Agrifoglio, E.A. Paez-Mozo, H. Arzoumanian, *Catal. Today* 133 (2008) 619–624.
- [37] C.A. Paez, O. Lozada, N.J. Castellanos, F.O. Martinez, F. Ziarelli, G. Agrifoglio, E.A. Paez-Mozo, H. Arzoumanian, *J. Mol. Catal. A: Chem.* 299 (2009) 53–59.
- [38] T. Szymanska-Buzar, *Coord. Chem. Rev.* 249 (2005) 2195–2202.
- [39] M. Stosur, T. Szymanska-Buzar, *J. Mol. Catal. A: Chem.* 286 (2008) 98–105.
- [40] M. Zyder, A. Kochel, T. Szymanska-Buzar, *J. Organomet. Chem.* 694 (2009) 4196–4203.
- [41] P.K. Baker, *Chem. Soc. Rev.* 27 (1998) 125–132.
- [42] W.M. Carmichael, D.A. Edwards, G.W.A. Fowles, P.R. Marshall, *Inorg. Chim. Acta* 1 (1967) 93–96.
- [43] C.D. Nunes, A.A. Valente, M. Pillinger, A.C. Fernandes, C.C. Romão, J. Rocha, I.S. Gonçalves, *J. Mater. Chem.* 12 (2002) 1735–1742.
- [44] M. Kruk, M. Jaroniec, *Langmuir* 13 (1997) 6267–6273.
- [45] M. Kruk, V. Antochshuk, M. Jaroniec, *J. Phys. Chem. B* 103 (1999) 10670–10678.
- [46] R.G. Parr, W. Yang, *Density Functional Theory of Atoms and Molecules*, University Press, Oxford, New York, 1989.
- [47] Gaussian 03, Revision C.02, http://www.gaussian.com/g_misc/g03/citation.g03.htm.
- [48] (a) A.D.J. Becke, *Chem. Phys.* 98 (1993) 5648–5652;
(b) C. Lee, W. Yang, G. Parr, *Phys. Rev. B* 37 (1988) 785–789.
- [49] (a) A.N.D. McLean, G.S. Chandler, *J. Chem. Phys.* 72 (1980) 5639–5648;
(b) R. Krishnan, J.S. Binkley, R. Seeger, J.A. Pople, *J. Chem. Phys.* 72 (1980) 650–654;
(c) A.J.H. Wachters, *J. Chem. Phys.* 52 (1970) 1033–1036;
(d) P.J. Hay, *J. Chem. Phys.* 66 (1977) 4377–4384;
(e) K. Raghavachari, G.W. Trucks, *J. Chem. Phys.* 91 (1989) 1062–1065;
(f) L.A. Curtiss, M.P. McGrath, J.-P. Blaudeau, N.E. Davis, R.C. Binning Jr., L. Radom, *J. Chem. Phys.* 103 (1995) 6104–6113;
(g) M.P. McGrath, L. Radom, *J. Chem. Phys.* 94 (1991) 511–516.
- [50] (a) R.E. Stratmann, G.E. Scuseria, M.J. Frisch, *J. Chem. Phys.* 109 (1998) 8218–8224;
(b) R. Bauernschmitt, R. Ahlrichs, *Chem. Phys. Lett.* 256 (1996) 454–464;
(c) M.E. Casida, C. Jamorski, K.C. Casida, D.R. Salahub, *J. Chem. Phys.* 108 (1998) 4439–4449.
- [51] E.D. Glendening, J.K. Badenhoop, A.E. Reed, J.E. Carpenter, J.A. Bohmann, C.M. Morales, F. Weinhold, NBO 5.0. program, Theoretical Chemistry Institute, University of Wisconsin, Madison, 2001.
- [52] J.A.A. Sales, A.G.S. Prado, C. Airoidi, *Polyhedron* 21 (2002) 2647–2651.
- [53] C.D. Nunes, M. Pillinger, A.A. Valente, I.S. Gonçalves, J. Rocha, P. Ferreira, F.E. Kühn, *Eur. J. Inorg. Chem.* 2002 (2002) 1100–1107.
- [54] N.U. Silva, C.I. Fernandes, T.G. Nunes, M.S. Saraiva, C.D. Nunes, P.D. Vaz, *Appl. Catal. A: Gen.* 408 (2011) 105–116.
- [55] B. Marler, U. Oberhagemann, S. Voltmann, H. Gies, *Microporous Mater.* 6 (1996) 375–383.
- [56] W. Hammond, E. Prouzet, S.D. Mahanti, T.J. Pinnavaia, *Microporous Mesoporous Mater.* 27 (1999) 19–25.
- [57] S.J. Gregg, K.S.W. Sing, *Adsorption, Surface Area and Porosity*, 2nd ed., Academic Press, London, 1982.
- [58] M.D. Alba, A. Becerro, J. Klinowski, *J. Chem. Soc., Faraday Trans.* 92 (1996) 849–854.
- [59] A.A. Romero, M.D. Alba, W. Zhou, J. Klinowski, *J. Phys. Chem. B* 101 (1997) 5294–5300.
- [60] M. Kruk, M. Jaroniec, *Langmuir* 15 (1999) 5410–5413.
- [61] (a) M. Cheng, W. Ma, C. Chen, J. Yao, J. Zhao, *Appl. Catal. B: Environ.* 65 (2006) 217–226;
(b) Z. He, S. Yang, Y. Ju, C. Sun, *J. Environ. Sci.* 21 (2008) 268–272;
(c) Z. He, C. Sun, S. Yang, Y. Ding, H. He, Z. Wang, *J. Hazard. Mater.* 162 (2009) 1477–1486.
- [62] M.H. Florêncio, E. Pires, A.L. Castro, M.R. Nunes, C. Borges, F.M. Costa, *Chemosphere* 55 (2004) 345–355.
- [63] J.-Y. Li, W.-H. Ma, P.-P. Lei, J.-C. Zhao, *J. Environ. Sci.* 19 (2007) 892–896.
- [64] Y. Li, Z. Yi, Y. Zhang, M. Wu, W. Lin, P. Duan, *J. Hazard. Mater.* 171 (2009) 1172–1174.